A framework for macroscale modelling of inelastic deformations in 3D-woven composites

(article starts on next page)

A framework for macroscale modelling of inelastic deformations in 3D-woven composites

Carolyn Oddy [a,*], Magnus Ekh [a], Tomas Ekermann [b], Stefan Hallström [b], Martin Fagerström [a]

[a] *Department of Industrial and Materials Science, Chalmers University of Technology, SE-412 96, Gothenburg, Sweden*
[b] *Department of Aeronautical and Vehicle Engineering, KTH Royal Institute of Technology, SE-100 44, Stockholm, Sweden*

ARTICLE INFO

ABSTRACT

The use of 3D-woven composite materials has shown promising results. Along with weight-efficient stiffness and strength, they have demonstrated encouraging out of plane properties, damage tolerance and energy absorption capabilities. The widespread adoption of 3D-woven composites in industry however, requires the development of efficient computational models that can capture the material behaviour. The following work proposes a framework for modelling the mechanical response of 3D-woven composites on the macroscale. This flexible and thermodynamically consistent framework, decomposes the stress and strain tensors into two main parts motivated by the material architecture. The first is governed by the material behaviour along the reinforcement directions while the second is driven by shear behaviours. This division allows for the straightforward addition and modification of various inelastic phenomena observed in 3D-woven composites.

In order to demonstrate the applicability of the framework, focus is given to predicting the material response of a 3D glass fibre reinforced epoxy composite. Prominent non-linearities are noted under shear loading and loading along the horizontal weft yarns. The behaviour under tensile loading along the weft yarns is captured using a Norton style viscoelasticity model. The non-linear shear response is introduced using a crystal plasticity inspired approach. Specifically, viscoelasticity is driven on localised slip planes defined by the material architecture. The viscous parameters are calibrated against experimental results and off axis tensile tests are used to validate the model.

1. Introduction

Traditional laminated fibre composites, in particular carbon fibre-reinforced polymers (CFRP), can provide high strength and stiffness relative to weight. Limitations however arise when it comes to components that must absorb energy or undergo excessive bending. Laminated composites that are loaded in this manner, are prone to significant delamination due to the low inter-laminar strength. In the event that delamination cracks form and propagate, a significant portion of the materialâs energy absorption capability is lost, as this damage mode consumes considerably less energy than e.g. crushing failure.

Composite materials with 3D-woven reinforcement may help to circumvent some of these challenges. Along with weight-efficient strength and stiffness characteristics, 3D-woven composites show a number of promising properties. Stig and Hallström (2009) for example have demonstrated that composites with 3D-textile reinforcement have improved mechanical out-of-plane properties in both tension and shear

when compared to their laminated 2D reinforced counterparts. This has also been discussed by Ansar et al. (2011) and references therein. Even more noteworthy, Khokar et al. (2015) have demonstrated that in four point bending, a 3D-CFRP I-beam has up to three times the specific energy absorption capability of a steel I-beam with equivalent geometry. The fibre networks suppress delamination and allow for stable and progressive damage growth in a quasi-ductile manner.

With respect to applications of 3D-woven composites in industry, additional requirements arise. Developing computational models of the mechanical material behaviour in particular is key to supporting their widespread adoption. Suitable modelling approaches are needed in order to predict the relevant mechanical material phenomena. These models must however be computationally efficient in order to assure industrial turnaround times and have a clear calibration procedure.

Existing modelling approaches for 3D-woven composites, often focus on the understanding of the complex material behaviour at the sub-scales. To this end, multiscale modelling techniques are commonly used.

Here, the hierarchical nature of woven composites is used to identify distinct length scales. The finest scale relevant for a continuum model, the microscale, consists of single fibre filaments embedded in the matrix material. One level up on the mesoscale, multiple filaments are grouped into various yarns that are arranged in a specific weaving architecture. The phenomena on the micro and mesoscale subsequently defines the effective material behaviour on the macroscale.

Early modelling approaches for 3D-woven composites focused mostly on predicting the link between mesoscale weave architectures and the material's macroscale elastic stiffness and strength values. Whitney and Chou (1988), Yushanov and Bogdanovic (1999) as well as Tong et al. (2002) all presented various analytical models to do just that. Many now turn to finite element (FE) approaches, which require the creation of a representative unit cell of the material's weave architecture. This in itself can be quite a challenging task as shown by Stig and Hallström (2012) as well as Lomov et al. (2000). Once a representative unit cell has been created, it is possible to predict more complex behaviours such as viscoelasticity of the matrix and yarns, see Hirsekorn et al. (2018), and progressive damage, see Lomov et al. (2007), Green et al. (2014). More recently El Said et al. (El Said et al., 2018) developed an iterative concurrent multiscale modelling approach to predict non-linear behaviour and progressive damage in 3D-woven composites.

Explicitly considering the reinforcement architecture of 3D-woven composites has its advantages. It allows for a detailed understanding and prediction of the mesoscale response. Modelling the behaviour of large structures however, with such detail, requires substantial modelling effort and computational resources. Another possibility then is to turn to macroscale phenomenologically based models. This includes models such as the ONERA Damage Model of Polymer Matrix Composites (Marcin et al., 2008) and that presented by Xia et al. (2002) for plastic deformations of paper. The ONERA Damage Model in particular has been developed to account for viscous effects, damage propagation and final failure of 3D-woven composites. Approximating the structural domain as a homogeneous material of orthotropic nature allows for a computationally efficient manner to model the mechanical behaviour of the material. The long-term goal of this work therefore involves developing a phenomenologically based macroscale model to predict how 3D-woven composites deform and eventually fail under loading. In particular it must predict the inelastic processes that lead to energy absorption.

The inherent nature of 3D-weaving techniques allow for the direct manufacturing of complex fibre preforms that can be strategically tailored to the overall needs of a desired component. The range of observed behaviours of 3D-woven composites can therefore vary drastically from one set of weave parameters to the next. 3D-woven composites have widely been shown to demonstrate prominent matrix driven non-linear behaviours when loaded in shear, cf. Ekermann and Hallström (2015) as well as Warren et al. (2015). The same general statement however can not be made when it comes to loading along the reinforcement directions. Dahale et al. (2019) for example, have demonstrated that denser weave patterns give a nearly linear stress-strain response when specimens are loaded in tension along the reinforcement directions. In contrast however, a composite with a less dense weave pattern showed more significant non-linearity due to straightening of heavily misaligned yarns. In a similar fashion, Stig and Hallström (2019) also noticed that while some 3D-woven specimens with nominally straight yarns behave linearly until failure when loaded along the reinforcements, others do not. Increased crimp in fibre tows can drive non-linear behaviours due to a phenomenon denoted by Cox et al. (1996) as plastic tow straightening. Developing a flexible foundation that allows for straightforward model additions and extensions to capture various experimentally observed behaviours would therefore be a promising step.

The following work presents a thermodynamically consistent model framework based on the use of structural tensors. It builds on a model for unidirectional composite plies first presented by Spencer (1984) and
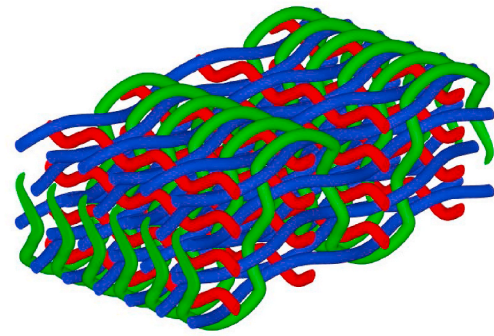

Fig. 1. Sketch of the 3D-woven reinforcement, created in TexGen (Brown and Sherburn, 2017). Blue yarns are warp, red and green yarns are horizontal and vertical weft respectively. (For interpretation of the references to colour in this figure legend, the reader is referred to the Web version of this article.)

later used by e.g. Nedjar (2011), Vogler et al. (2013), Camanho et al. (2015) and Nagaraja et al. (2019) and extends it to 3D-woven composites. The proposed framework decomposes the stress and strain tensors into two main parts. This conveniently allows for the separation of reinforcement driven phenomena and shear or off-axis driven phenomena. In particular, the separation makes it possible to incorporate pronounced non-linear dissipative material behaviour in shear, observed for 3D-woven composites. It also allows for the inclusion of non-linear behaviour in one or multiple reinforcement directions. Various inelastic formulations (viscoelastic, plastic, and viscoplastic) can be chosen and included based on the behaviour in each material direction. It also implies that separate behaviours can be included in different loading directions. Among other benefits, this simplifies material parameter identification.

In the present contribution the proposed framework is applied to the specific case of a fully 3D glass fibre reinforced epoxy composite. Focus is given to capturing both the non-linear shear behaviour demonstrated by the considered material as well as the non-linear behaviour shown when loaded along one of the reinforcement directions. A Norton style (Norton, 1929) viscoelasticity model is used to capture the reinforcement related non-linearity. The non-linear shear response in particular however is introduced using a crystal plasticity inspired approach (Hill, 1966). In more detail, it is assumed that viscoelastic slip is localised to planes determined by the reinforcement architecture. Further, the development of the viscoelastic strain is driven by the shear component of the traction vector on each plane. The use of a crystal plasticity inspired approach also makes it possible to independently tailor the viscous parameters in each slip plane. The viscous parameters are calibrated against experimental results and it is shown that the calibrated model is able to predict the material behaviour under off-axis tensile loading.

2. Considered material

A sketch of a typical construct of the considered class of 3D-woven reinforcement is presented in Fig. 1. This weaving technique, described by Khokar (2001) and produced by Biteam AB, allows for the direct manufacturing of complex fibre preforms with various cross section geometries that can be tailored to the overall needs of the desired component. It consists of three sets of yarns: warp yarns (blue) extending in the weaving direction as well as horizontal weft (red) and vertical weft (green) yarns extending transversely to the weave in the width and thickness directions respectively.

Preliminary experimental results for a 3D glass fibre reinforced epoxy composite are shown in Figs. 2 and 3a. They are discussed in greater detail in Section 5. Fig. 2a shows the stress strain response of tensile loading along the warp yarns - the stiffest and strongest direction. It exhibits a (nearly) linear response up until failure. The same however
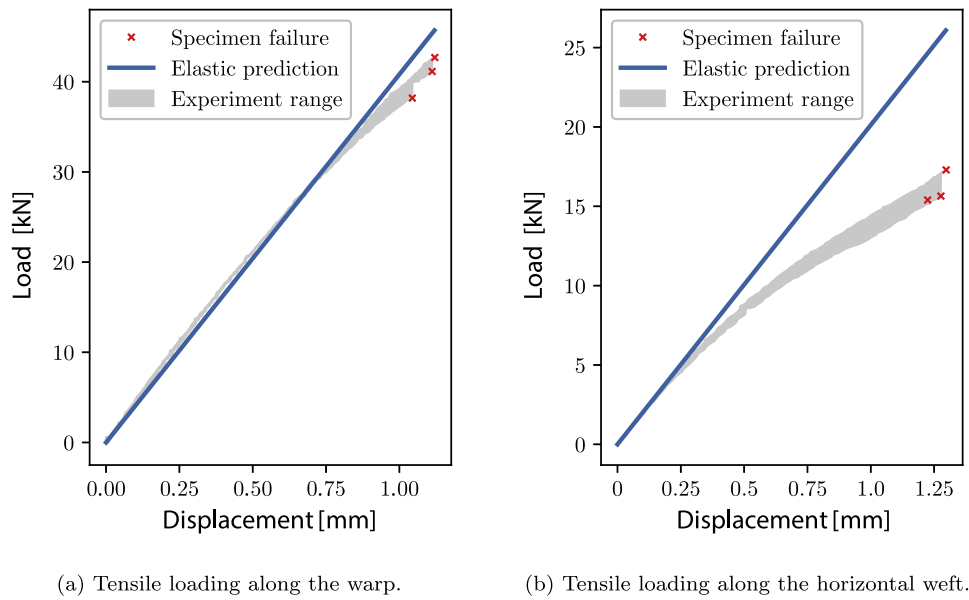
(a) Tensile loading along the warp.

(b) Tensile loading along the horizontal weft.

Fig. 2. Preliminary load-displacement curves of tensile specimens.

(a) In plane shear loading.

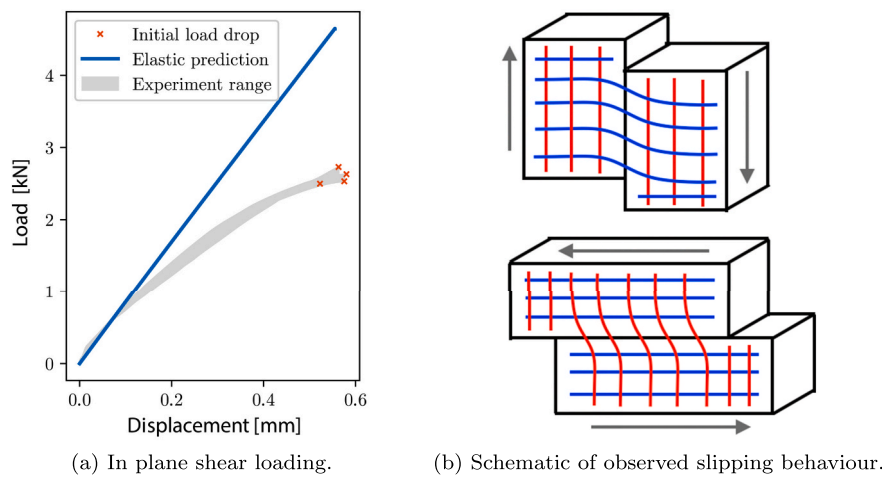(b) Schematic of observed slipping behaviour.

Fig. 3. Preliminary load-displacement curve for shear specimen and schematic of shear slipping behaviour.

can not be said for loading along all reinforcement directions. Tensile loading in the direction of the horizontal weft reinforcements, illustrated in Fig. 2b, shows a notable non-linear response. In-plane shear loading, shown in Fig. 3a until the first load drop, also produces a prominent initial non-linear response as well as deformation modes with a preference for slip in certain planes defined by the reinforcement architecture, illustrated schematically in Fig. 3b. This observed non-linearity is likely due to the viscoelastic behaviour and eventual damage of the matrix (Marcin et al., 2008). Accounting for these non-linear behaviours is an essential first step to developing an accurate computational model of the overall behaviour of this class of material.

3. Model framework formulation

As a first step, the following section presents a macroscale framework for modelling 3D-woven composites. The framework is thermodynamically consistent and convenient to extend to a large strain setting. It also allows for the adoption of various inelastic models that can be tailored to the needs of a given material. First, in Section 3.1 work initially carried out by Spencer (1984) for unidirectional composites is reviewed. His proposed model is then extended to the case of 3D-woven composites in Section 3.2. The thermodynamic perspective of the model is also discussed in preparation for inelastic model additions in Section 4.

3.1. Decomposition of stress and strain tensors for unidirectional composites

In Spencer (1984) Spencer focuses on continuum theories that describe the macroscopic behaviour of fibre-reinforced materials. In particular he proposes a method to decompose the stress tensor in a way that allows for the separation of behaviour in the reinforcement directions from behaviour under off-axis or shear loading. This decomposition has later been utilised by e.g. Nedjar (2011), Vogler et al. (2013), and Camanho et al. (2015). They, respectively, used the proposed decomposition to develop a viscoelasticity model, a plasticity model as well as three-dimensional failure criteria for transversely

isotropic unidirectional composites.

Traditional unidirectional composites contain a single family of reinforcement fibres which creates an anisotropic material behaviour with a single preferred direction. Starting from such a unidirectional fibre-reinforced material in which the reinforcement fibres are oriented along a vector a, Spencer proposed the following decomposition of the stress tensor,

$$\boldsymbol{\sigma} = \boldsymbol{s} + p\boldsymbol{1} + T\boldsymbol{A}, \tag{1}$$

where $\boldsymbol{1}$ denotes the second order identity tensor and $\boldsymbol{A}$ the second order structural tensor defined as

$$\boldsymbol{A} = \boldsymbol{a} \otimes \boldsymbol{a}. \tag{2}$$

Conceptually speaking, this means that the final term contains components in the main reinforcement direction, while the middle term contains a contribution of volumetric nature. The first term consists of the remaining stress components.

Explicit expressions for p and T are found by considering constraints on $\boldsymbol{s}$. Firstly, in order to ensure that $\boldsymbol{s}$ is completely void of any hydrostatic stress contribution $\boldsymbol{s}$ must be deviatoric, i.e.

$$\boldsymbol{s} : \boldsymbol{1} = 0. \tag{3}$$

Secondly, the conditions that $\boldsymbol{s}$ has no contribution in the reinforcement direction is given by

$$\boldsymbol{s} : \boldsymbol{A} = 0. \tag{4}$$

By combining Equations (1), (3) and (4), it can be shown that

$$p = \frac{1}{2}(\mathrm{tr}[\boldsymbol{\sigma}] - [\boldsymbol{\sigma} : \boldsymbol{A}]) \tag{5}$$

$$T = \frac{1}{2}(3[\boldsymbol{\sigma} : \boldsymbol{A}] - \mathrm{tr}[\boldsymbol{\sigma}]), \tag{6}$$

where $\mathrm{tr}[\bullet] = \bullet : \boldsymbol{1}$ is the trace of $\bullet$.

For clarity, consider a material with a fibre direction running along the first main axis, i.e. $\boldsymbol{a} = [1\ 0\ 0]^T$. The proposed stress decomposition becomes

$$\boldsymbol{\sigma} = \underbrace{\begin{bmatrix} 0 & \sigma_{12} & \sigma_{13} \\ \sigma_{12} & \frac{1}{2}(\sigma_{22} - \sigma_{33}) & \sigma_{23} \\ \sigma_{13} & \sigma_{23} & \frac{1}{2}(-\sigma_{22} + \sigma_{33}) \end{bmatrix}}_{s} + \underbrace{\frac{1}{2}(\sigma_{22} + \sigma_{33})}_{p}\begin{bmatrix} 1 & 0 & 0 \\ 0 & 1 & 0 \\ 0 & 0 & 1 \end{bmatrix}$$
$$+ \underbrace{\left(\sigma_{11} - \frac{1}{2}(\sigma_{22} + \sigma_{33})\right)}_{T}\begin{bmatrix} 1 & 0 & 0 \\ 0 & 0 & 0 \\ 0 & 0 & 0 \end{bmatrix}. \tag{7}$$

When it comes to the strain tensor, Nedjar (2011) later showed that for transversely isotropic composite materials (again with fibres aligned along $\boldsymbol{a}$), it is also convenient to decompose it as follows

$$\boldsymbol{\varepsilon} = \boldsymbol{e} + \zeta\boldsymbol{1} + \xi\boldsymbol{A}. \tag{8}$$

In a synonymous way to that of the stress tensor, $\boldsymbol{e}$ is assumed to fulfil

$$\boldsymbol{e} : \boldsymbol{1} = 0, \tag{9}$$

$$\boldsymbol{e} : \boldsymbol{A} = 0, \tag{10}$$

from which explicit expressions for ζ and ξ can be derived. Due to the decompositions of stress and strain it follows directly that $\boldsymbol{s}$ and $\boldsymbol{e}$ are energy conjugated. Furthermore, by imposing this strain decomposition and linear elastic transverse isotropy it is shown in Nedjar (2011) that $\boldsymbol{s}$ only depends on $\boldsymbol{e}$ and not on the total strain $\boldsymbol{\varepsilon}$, i.e.

$$\boldsymbol{s} = \boldsymbol{s}(\boldsymbol{e}). \tag{11}$$

Notably, the lack of coupling between the shear, volumetric and reinforcement related parts of the strain and stress tensors has a number of positive advantages. It becomes possible to identify and incorporate material behaviours in the appropriate parts in a physically meaningful way. Again, this fact has been exploited by e.g. Nedjar (2011), Vogler (Vogler et al., 2013) and Camanho (Camanho et al., 2015).

3.2. Modelling framework for 3D-woven composites

Extending these decompositions to the considered 3D-woven material allows for a generic framework that provides many possibilities for further model developments and additions. Specifically, it allows for the convenient separation of matrix-related and reinforcement-related material behaviours. The following section begins by reviewing a structural tensor based formulation of the elastic stiffness tensor. This is followed by the extension of the stress and strain decomposition to 3D-woven composites.

3.2.1. Elastic orthotropy

The nature of 3D-woven reinforcement produces a material with three preferred directions, each having their own unique properties. Modelling this class of material therefore requires the use of a fully orthotropic stiffness tensor. One way to express the stiffness tensor is through the use of 9 elastic engineering parameters, specifically: Young's moduli, shear moduli and Poisson's ratios. In Voigt form this relationship can be expressed as

$$\begin{bmatrix} \varepsilon_{11} \\ \varepsilon_{22} \\ \varepsilon_{33} \\ \gamma_{12} \\ \gamma_{23} \\ \gamma_{13} \end{bmatrix} = \begin{bmatrix} 1/E_{11} & -\nu_{21}/E_{22} & -\nu_{31}/E_{33} & 0 & 0 & 0 \\ -\nu_{12}/E_{11} & 1/E_{22} & -\nu_{32}/E_{33} & 0 & 0 & 0 \\ -\nu_{13}/E_{11} & -\nu_{23}/E_{22} & 1/E_{33} & 0 & 0 & 0 \\ 0 & 0 & 0 & 1/G_{12} & 0 & 0 \\ 0 & 0 & 0 & 0 & 1/G_{23} & 0 \\ 0 & 0 & 0 & 0 & 0 & 1/G_{13} \end{bmatrix} \begin{bmatrix} \sigma_{11} \\ \sigma_{22} \\ \sigma_{33} \\ \sigma_{12} \\ \sigma_{23} \\ \sigma_{13} \end{bmatrix} \tag{12}$$

Defining the orthotropic stiffness tensor through the use of structural tensors instead however, has a number of advantages. It provides a convenient, flexible formulation which allows for local variations in reinforcement orientation at each material point without the need to transform to a local coordinate system.

Consider an orthotropic material with three preferred directions, i.e. the reinforcement directions in Fig. 1, defined by the mutually orthogonal vectors $\boldsymbol{a}^I$ for $I = 1, 2, 3$. By introducing three associated second order structural tensors

$$\boldsymbol{A}^I = \boldsymbol{a}^I \otimes \boldsymbol{a}^I \text{ for } I = 1, 2, 3, \tag{13}$$

the fourth order orthotropic stiffness tensor can be expressed as

$$\mathbb{E} = \sum_{I=1}^{3} 3\phi_I \mathbb{A}^I + \sum_{I=1}^{3}\sum_{J=1}^{3} 3\varphi_{IJ}\boldsymbol{A}^I \otimes \boldsymbol{A}^J. \tag{14}$$

Here the fourth order tensor $\mathbb{A}^I$ is given by [1]

$$\mathbb{A}^I = \frac{1}{2}\left(\boldsymbol{A}^I \overline{\otimes} \boldsymbol{1} + \boldsymbol{1}\overline{\otimes}\boldsymbol{A}^I\right) \tag{15}$$

To help visualise Equation (14), Equation (16) shows the obtained stiffness tensors in Voigt form for the case where the three preferred directions correspond to $\boldsymbol{a}^1 = [1\ 0\ 0]^T$, $\boldsymbol{a}^2 = [0\ 1\ 0]^T$ and $\boldsymbol{a}^3 = [0\ 0\ 1]^T$ respectively. Note that although this structural tensor-based representation of the orthotropic elastic stiffness does not directly involve the elastic engineering parameters, it is possible to relate the coefficients ϕ_I and φ_{IJ} to them. This is possible by considering the case where the three reinforcement directions correspond to the main coordinate axes, i.e. by comparing Equations (16) and (12).

---

[1] The nonstandard $\overline{\otimes}$ operator expresses the operation $(\boldsymbol{A}\overline{\otimes}\boldsymbol{B})_{ijkl} = A_{ik}B_{jl}$

$$\mathbb{E} = \begin{bmatrix} \varphi_{11}+\phi_1 & \varphi_{12} & \varphi_{13} & 0 & 0 & 0 \\ \varphi_{12} & \varphi_{22}+\phi_2 & \varphi_{23} & 0 & 0 & 0 \\ \varphi_{13} & \varphi_{23} & \varphi_{33}+\phi_3 & 0 & 0 & 0 \\ 0 & 0 & 0 & 1/4(\phi_1+\phi_2) & 0 & 0 \\ 0 & 0 & 0 & 0 & 1/4(\phi_2+\phi_3) & 0 \\ 0 & 0 & 0 & 0 & 0 & 1/4(\phi_3+\phi_1) \end{bmatrix} \tag{16}$$

Finally, using the considered structural tensors, the constitutive stress-strain relationship for elastic orthotropy can be expressed as

$$\boldsymbol{\sigma} = \sum_{I=1}^{3} \phi_I \mathbb{A}^I : \boldsymbol{\varepsilon} + \sum_{I=1}^{3}\sum_{J=1}^{3} \varphi_{IJ}\left(\boldsymbol{A}^J:\boldsymbol{\varepsilon}\right)\boldsymbol{A}^I, \tag{17}$$

where $\varphi_{IJ} = \varphi_{JI}$.

3.2.2. Decomposition of the stress tensor

In his work, Spencer (1984) indicated that by following the same thought process and procedures, his methodology can be used beyond unidirectional composites to describe the macroscopic behaviour of increasingly complex fibre-reinforced materials. In the case of the considered 3D-woven composite, the stress decomposition would then become

$$\boldsymbol{\sigma} = \boldsymbol{s} + p\boldsymbol{I} + \sum_{I=1}^{3} T^I \boldsymbol{A}^I. \tag{18}$$

In a synonymous way to the decomposition presented in Equation (1), Equation (18) for 3D reinforcements holds a term with the remaining off-axis components, a term of volumetric nature and terms containing the components related to the three reinforcement directions.

Expressions for the coefficients p and T^I may again be determined through assumptions on $\boldsymbol{s}$. Specifically that $\boldsymbol{s}$ is assumed to be deviatoric and contain no volumetric components or components in the reinforcement directions, i.e

$$\boldsymbol{s}:\boldsymbol{I} = 0 \text{ and } \boldsymbol{s}:\boldsymbol{A}^I = 0, \text{ for } I = 1,2,3. \tag{19}$$

In the considered 3D-woven composite, the three reinforcement directions are mutually orthogonal, meaning that

$$\boldsymbol{A}^1 + \boldsymbol{A}^2 + \boldsymbol{A}^3 = \boldsymbol{I}. \tag{20}$$

Under these circumstances, p and T^I in Equation (18) cannot be uniquely determined from the constraints on $\boldsymbol{s}$ in Equation (19).[2] Therefore a simplification to Equation (18) is proposed as the following decomposition

$$\boldsymbol{\sigma} = \boldsymbol{s} + \sum_{I=1}^{3} 3T^I \boldsymbol{A}^I. \tag{21}$$

Then T^I can be determined from the three constraints

$$\boldsymbol{s}:\boldsymbol{A}^I = 0, \text{ for } I = 1,2,3, \tag{22}$$

resulting in

$$T^I = \boldsymbol{\sigma}:\boldsymbol{A}^I. \tag{23}$$

This means that, in the final form given by Equations (21) and (23),

the normal stress components solely influence the behaviour in the reinforcement directions and do not influence the shear response.

For clarity, consider the decomposition given in Equations (21) and (23) for a material point in which the local yarn orientations are given by the principal coordinate axes. That is again where $\boldsymbol{a}^1 = [1\ 0\ 0]^T$, $\boldsymbol{a}^2 = [0\ 1\ 0]^T$ and $\boldsymbol{a}^3 = [0\ 0\ 1]^T$. This gives (in matrix form) that

$$\boldsymbol{\sigma} = \underbrace{\begin{bmatrix} 0 & \sigma_{12} & \sigma_{13} \\ \sigma_{12} & 0 & \sigma_{23} \\ \sigma_{13} & \sigma_{23} & 0 \end{bmatrix}}_{s} + \underbrace{\begin{bmatrix} \sigma_{11} & 0 & 0 \\ 0 & 0 & 0 \\ 0 & 0 & 0 \end{bmatrix}}_{T^1 A^1} + \underbrace{\begin{bmatrix} 0 & 0 & 0 \\ 0 & \sigma_{22} & 0 \\ 0 & 0 & 0 \end{bmatrix}}_{T^2 A^2} + \underbrace{\begin{bmatrix} 0 & 0 & 0 \\ 0 & 0 & 0 \\ 0 & 0 & \sigma_{33} \end{bmatrix}}_{T^3 A^3}. \tag{24}$$

The stress is then again decomposed into one term driven by the shear stresses in the material ($\boldsymbol{s}$) and three terms driven by the stresses along the three reinforcement directions. Finally, through Equations (21) and (23) it is possible to relate $\boldsymbol{s}$ to $\boldsymbol{\sigma}$ through the fourth order projection tensor $\mathbb{Q}$, i.e.

$$\boldsymbol{s} = \mathbb{Q}:\boldsymbol{\sigma} \tag{25}$$

where

$$\mathbb{Q} = \mathbb{I} - \sum_{I=1}^{3} 3\boldsymbol{A}^I \otimes \boldsymbol{A}^I, \tag{26}$$

and $\mathbb{I}$ is the fourth order identity tensor. In a similar fashion as for the stress, the strain can be decomposed as follows for three mutually orthogonal reinforcement directions

$$\boldsymbol{\varepsilon} = \boldsymbol{e} + \sum_{I=1}^{3} \left(\boldsymbol{\varepsilon}:\boldsymbol{A}^I\right)\boldsymbol{A}^I, \tag{27}$$

where now

$$\boldsymbol{e}:\boldsymbol{I} = 0 \text{ and } \boldsymbol{e}:\boldsymbol{A}^I = 0, \text{ for } I = 1,2,3. \tag{28}$$

In a synonymous way as for the stress, the first term in the decomposition given by Equation (26), holds the shear strain components while the final three terms hold the strain components in the reinforcement directions.

The full strain tensor $\boldsymbol{\varepsilon}$ and $\boldsymbol{e}$ may again be related to each other through the projection tensor given by Equation (24), where

$$\boldsymbol{e} = \mathbb{Q}:\boldsymbol{\varepsilon}.$$

3.2.3. General constitutive framework

What remains is to fully define the constitutive relationship of the material according to the proposed stress and strain decompositions given by Equations (21) and (27). Firstly, the relationship between $\boldsymbol{s}$ and $\boldsymbol{e}$ can by determined by combining Equations (25) and (17), i.e.

$$\boldsymbol{s} = \mathbb{Q}:\boldsymbol{\sigma} = \sum_{I=1}^{3} 3\phi_I \mathbb{A}^I : \boldsymbol{e}. \tag{29}$$

It is then possible to express the stresses along the reinforcement directions (T^I) as

$$T^I = \boldsymbol{\sigma}:\boldsymbol{A}^I = \phi_I\left(\boldsymbol{A}^I:\boldsymbol{\varepsilon}\right) + \sum_{J=1}^{3} \varphi_{IJ}\left(\boldsymbol{A}^J:\boldsymbol{\varepsilon}\right) \tag{30}$$

---

[2] The constraint $\boldsymbol{s}:\boldsymbol{1} = 0$ will be automatically fulfilled when $\boldsymbol{s}:\boldsymbol{A}^I = \boldsymbol{0}$ for $I = 1,2,3$. Thus, only three independent constraints remain, which is insufficient to uniquely determining p and T^I.

Note that it again has been advantageously shown that s and e can be directly related to one another without any additional coupling to other strain components. The stress–strain relations in Equations (29) and (30) are also possible to formulate in the following form

$$\boldsymbol{\sigma} = \mathbb{E}_{\mathrm{m}} : \boldsymbol{e} + \mathbb{E}_{\mathrm{f}} : \boldsymbol{\varepsilon}, \tag{31}$$

where

$$\mathbb{E}_{\mathrm{m}} = \sum_{I=1}^{3} 3\phi_I \mathbb{A}^I, \text{ and } \mathbb{E}_{\mathrm{f}} = \sum_{I=1}^{3} 3\left(\phi_I \boldsymbol{A}^I \otimes \boldsymbol{A}^I + \sum_{J=1}^{3} 3\varphi_{IJ} \boldsymbol{A}^I \otimes \boldsymbol{A}^J\right). \tag{32}$$

3.2.4. Thermodynamic perspective

From a thermodynamics perspective, the relationships presented in the previous sections can also be derived. Beginning from the free energy for a linear elastic orthotropic material, given by

$$\Psi = \frac{1}{2}\sum_{I=1}^{3} \phi_I \boldsymbol{A}^I : \boldsymbol{\varepsilon}^2 + \frac{1}{2}\sum_{I=1}^{3}\sum_{J=1}^{3} \varphi_{IJ}\left(\boldsymbol{A}^I : \boldsymbol{\varepsilon}\right)\left(\boldsymbol{A}^J : \boldsymbol{\varepsilon}\right), \tag{33}$$

where $\boldsymbol{\varepsilon}^2 = \boldsymbol{\varepsilon}\cdot\boldsymbol{\varepsilon}$, the constitutive stress–strain relationship for orthotropy, Equation (17), can be found given that $\boldsymbol{\sigma} = \partial\Psi/\partial\boldsymbol{\varepsilon}$. Furthermore, by considering the strain decomposition given by Equation (26) and inserting it into (32), the free energy can also be rewritten as

$$\Psi = \Psi_{\mathrm{e}}(\boldsymbol{e}) + \sum_{I=1}^{3} \Psi_{\varepsilon}^I\left(\boldsymbol{A}^J : \boldsymbol{\varepsilon}\right), \tag{34}$$

where

$$\Psi_{\mathrm{e}}(\boldsymbol{e}) = \frac{1}{2}\sum_{I=1}^{3} \phi_I \boldsymbol{A}^I : \boldsymbol{e}^2 \quad \text{and} \quad \Psi_{\varepsilon}^I\left(\boldsymbol{\varepsilon} : \boldsymbol{A}^J\right) = \frac{1}{2}\phi_I\left(\boldsymbol{A}^I : \boldsymbol{\varepsilon}\right)^2$$
$$+ \frac{1}{2}\sum_{J=1}^{3} \varphi_{IJ}\left(\boldsymbol{A}^I : \boldsymbol{\varepsilon}\right)\left(\boldsymbol{A}^J : \boldsymbol{\varepsilon}\right) \tag{35}$$

The constitutive relationships presented in Equations (29) and (30) then follow from the consideration of the dissipation equality for elasticity, i.e.

$$\mathscr{D} = \boldsymbol{\sigma} : \dot{\boldsymbol{\varepsilon}} - \dot{\Psi} = 0. \tag{36}$$

The first term, taking into account the aforementioned stress and strain decompositions, i.e. Equations (21) and (27), is then given by

$$\boldsymbol{\sigma} : \dot{\boldsymbol{\varepsilon}} = \boldsymbol{s} : \dot{\boldsymbol{e}} + \sum_{I=1}^{3}\left(\boldsymbol{A}^I : \boldsymbol{\sigma}\right)\left(\boldsymbol{A}^I : \dot{\boldsymbol{\varepsilon}}\right) \tag{37}$$

The time derivative of the free energy then follows from

$$\dot{\Psi} = \frac{\partial\Psi_e}{\partial\boldsymbol{e}} : \dot{\boldsymbol{e}} + \sum_{I=1}^{3}\sum_{J=1}^{3} \frac{\partial\Psi_{\varepsilon}^I}{\partial\left(\boldsymbol{A}^J : \boldsymbol{\varepsilon}\right)}\left(\boldsymbol{A}^J : \dot{\boldsymbol{\varepsilon}}\right) \tag{38}$$

In order to satisfy Equation (34), i.e. that there is no dissipation, the following must hold:

$$\boldsymbol{s} = \frac{\partial\Psi_e}{\partial\boldsymbol{e}} = \sum_{I=1}^{3} 3\phi_I \mathbb{A}^I : \boldsymbol{e} \tag{39}$$

and

$$\boldsymbol{A}^I : \boldsymbol{\sigma} = \sum_{J=1}^{3} \frac{\partial\Psi_{\varepsilon}^J}{\partial\left(\boldsymbol{A}^I : \boldsymbol{\varepsilon}\right)} = \phi_I\left(\boldsymbol{A}^I : \boldsymbol{\varepsilon}\right) + \sum_{J=1}^{3} \varphi_{IJ}\left(\boldsymbol{A}^J : \boldsymbol{\varepsilon}\right) \tag{40}$$

Lending more strength to the argument for the proposed decomposition of the stress and strain tensor, it can be seen that s and e are energy conjugated.
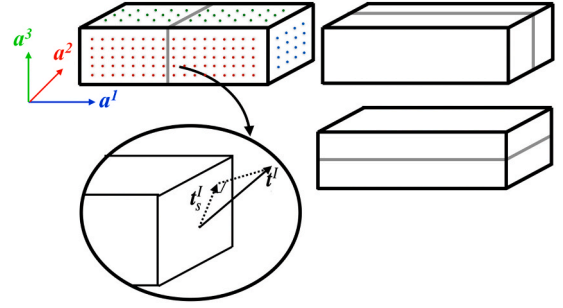

Fig. 4. Illustration of the considered slip planes and shear traction vector.

4. Model additions to capture inelastic phenomena

As previously discussed, the proposed decompositions of the stress and strain tensors, allow for the separation of reinforcement-related behaviours and shear-related behaviours. In the following sections, methods with which to include various experimentally observed non-linear behaviours in a modular fashion are proposed. In particular, focus is given to capturing the shear related non-linearity and weft reinforcement related non-linearity discussed in Section 2 for the considered 3D glass fibre reinforced epoxy.

4.1. Adding shear related non-linearity

Given the nature of the proposed decomposition, it is then natural to assume a shear-related inelastic behaviour only through the relation between s and e. Inspired by Nedjar (2011), it is proposed that e be additively decomposed into an elastic and an inelastic part,

$$\boldsymbol{e} = \boldsymbol{e}_{el} + \boldsymbol{e}_i. \tag{41}$$

The addition of inelastic behaviour means that the stress–strain relationship in Equation (53) transforms into

$$\boldsymbol{\sigma} = \mathbb{E}_{\mathrm{m}} : \left(\boldsymbol{e} - \boldsymbol{e}_i\right) + \mathbb{E}_{\mathrm{f}} : \boldsymbol{\varepsilon}. \tag{42}$$

The evolution of the inelastic shear strain, $\dot{\boldsymbol{e}}_i$ is likely governed by the behaviour of the matrix. Further, epoxy matrix systems have been shown to demonstrate strain-rate dependent viscoelastic behaviours, see for example Woo et al. (1991), and Saseendran (Saseendran et al., 2016). The resulting behaviour observed when the material is loaded along the reinforcement direction however must also be preserved. A model inspired by crystal plasticity (Hill, 1966) with viscoelastic slip planes is therefore considered. As such, it is assumed that viscoelastic strain should strictly develop when there is shear traction, t_s^I, in preferred material planes. This is similar to the ideas in a plasticity model presented by Larijani (Larijani et al., 2013) for pearlitic steel. These planes, illustrated by grey lines in Fig. 4, are defined by their respective normal vectors aligned with the nominal direction of the reinforcement architecture, i.e. the warp ($\boldsymbol{a}^1$), horizontal weft ($\boldsymbol{a}^2$) and vertical weft ($\boldsymbol{a}^3$) yarns cf. Fig. 1.

To restrict the development of shear-related viscoelastic strain to the preferred planes, and to mimic the monotonic load response as observed in the experiments, the following Norton type model is considered

$$\dot{\boldsymbol{e}}^i = \sum_{I=1}^{3} \underbrace{\frac{1}{t_*^I}\left(\frac{\left|t_s^I\right|}{\kappa^I}\right)^{n^I}}_{magnitude} \underbrace{\boldsymbol{m}^I}_{direction}. \tag{43}$$

The magnitude of the viscoelastic slip rate is driven by the magnitude of the shear traction, $\left|t_s^I\right|$, on each slip plane. In this model, t_*^I, n^I and κ^I are all parameters that control the non-linear viscous behaviour of the model.

Although in the simplest case these parameters are assumed to be the same and constant for each slip plane, we note that they may depend on the slip plane and may also be considered to evolve during the

deformation. For example, in the event that experimental testing shows a strong dependence between hydrostatic or transverse tensile/compressive loading and the shear behaviour of the material, a modification to κ could be introduced. In such a case, κ could be made dependent on the normal traction in each slip plane. Thus, the proposed framework is flexible and allows for the possible choice of other inelastic models as experimental results become available.

Note that the shear traction vectors, t_s^I, can be conveniently formulated given that

$$t_s^I = \boldsymbol{\sigma} \cdot \boldsymbol{a}^I - \left(\boldsymbol{\sigma} : \boldsymbol{A}^I\right) \boldsymbol{a}^I. \tag{44}$$

Its norm, can therefore be expressed as

$$\left|t_s^I\right| = \sqrt{\boldsymbol{s} : \mathbb{A}^I : \boldsymbol{s}}, \tag{45}$$

or equivalently

$$\left|t_s^I\right| = \sqrt{\boldsymbol{\sigma} : \mathbb{D}^I : \boldsymbol{\sigma}}, \tag{46}$$

where $\mathbb{D}^I$ is defined by

$$\mathbb{D}^I = \mathbb{A}^I - \boldsymbol{A}^I \otimes \boldsymbol{A}^I. \tag{47}$$

At this point, we also want to emphasise that the choice of letting $\boldsymbol{s}$ drive the development of the inelastic strain (through its projection on the shear planes) can also be motivated from a thermodynamics perspective. This is discussed in detail in Section 4.3.

Furthermore, the direction of the viscoelastic strain evolution is chosen to be of associative type, where

$$\boldsymbol{m}^I = \frac{\partial \left|t_s^I\right|}{\partial \boldsymbol{s}} = \frac{\mathbb{A}^I : \boldsymbol{s}}{\sqrt{\boldsymbol{s} : \mathbb{A}^I : \boldsymbol{s}}}. \tag{48}$$

This can also be expressed as

$$\boldsymbol{m}^I = \frac{\mathbb{D}^I : \boldsymbol{\sigma}}{\sqrt{\boldsymbol{\sigma} : \mathbb{D}^I : \boldsymbol{\sigma}}}.$$

The proposed model can also be extended with non-associative evolution laws if experimental data shows that it is necessary, cf. Vogler et al. (2013). Note that $\boldsymbol{m}^I$ defined in Equation (48) has the same property as $\boldsymbol{e}$, i.e.

$$\boldsymbol{m}^I : \boldsymbol{A}^J = 0 \quad \forall I, J = 1, 2, 3 \tag{49}$$

and therefore only has components in the slip planes.

4.2. Adding reinforcement related non-linearity

In order to include reinforcement-related behaviours into the modelling framework, such as those seen in the considered 3D glass fibre reinforced epoxy discussed in Section 2, an additive decompositions of the strain tensor is again considered. As such

$$\boldsymbol{\varepsilon} = \boldsymbol{\varepsilon}_{el} + \boldsymbol{\varepsilon}_i, \tag{50}$$

where $\boldsymbol{\varepsilon}_{el}$ and $\boldsymbol{\varepsilon}_i$ denote the elastic and inelastic parts of the full strain tensor, respectively. The nature of the framework allows for the flexible inclusion of inelastic behaviours in a single or multiple reinforcement directions. The considered material however, shows prominent non-linear behaviour when loading is applied in the same direction as the horizontal weft yarns ($\boldsymbol{a}^2$), cf. Fig. 2b. This however is not the case for all reinforcement directions. Tensile loading along the warp, see Fig. 2a, produced a (nearly) linear response up until failure.

In order to drive the non-linear behaviour strictly when the material is loaded along the horizontal weft reinforcements, it is proposed that the contribution to the inelastic strain tensor be constructed using

structural tensors. In this case, the considered direction is defined by the horizontal weft, i.e. $\boldsymbol{a}^2$. The reinforcement related inelastic contribution to the strain tensor can then be constructed as $\varepsilon_v \boldsymbol{A}^2$. Therefore, taking the shear related contribution discussed in Section 4.1 into account as well gives that

$$\boldsymbol{\varepsilon}_i = \boldsymbol{e}_i + \varepsilon_v \boldsymbol{A}^2. \tag{51}$$

The stress-strain constitutive relationship in Equation may then be expressed as

$$\boldsymbol{\sigma} = \mathbb{E} : (\boldsymbol{\varepsilon} - \boldsymbol{\varepsilon}_i), \tag{52}$$

which, due to the nature of the construction of $\mathbb{E}_m$ and $\mathbb{E}_f$ can be further expanded to

$$\boldsymbol{\sigma} = \mathbb{E}_m : (\boldsymbol{e} - \boldsymbol{e}_i) + \mathbb{E}_f : (\boldsymbol{\varepsilon} - \boldsymbol{\varepsilon}_i) \tag{53}$$

$$= \mathbb{E}_m : (\boldsymbol{e} - \boldsymbol{e}_i) + \mathbb{E}_f : (\boldsymbol{\varepsilon} - \varepsilon_v \boldsymbol{A}^2) \tag{54}$$

The observed reinforcement-related non-linearity is likely due to the movement of the weft yarns inside the polymer matrix. One possible formulation for the development of the inelastic strain, $\dot{\varepsilon}_v$, is again a Norton type viscoelasticity model. The nature of the framework however allows for the modification of this choice as experimental results become available.

As in the previous section, a choice must be made when it comes to the component that is used to drive the development of $\dot{\varepsilon}_v$. This is discussed from a thermodynamics perspective in Section 4.3. Conceptually however, one can consider that the magnitude of the development of the viscoelastic strain should only be driven by loads in the direction of the horizontal weft reinforcement, i.e. $\boldsymbol{\sigma} : \boldsymbol{A}^2$. Further, the direction of the evolution of the viscoelasticity is defined by the direction of the loading.

The evolution of the reinforcement related viscoelastic strain, $\dot{\varepsilon}_v$, may then be defined by

$$\dot{\varepsilon}_v = \underbrace{\frac{1}{t_s^r} \left(\frac{\left|\boldsymbol{\sigma} : \boldsymbol{A}^2\right|}{\kappa^r}\right)^{n^r}}_{magnitude} \underbrace{\mathrm{sgn}\left(\boldsymbol{\sigma} : \boldsymbol{A}^2\right)}_{direction}, \tag{55}$$

where t_s^r, κ^r and n^r are calibrated parameters used to fit the model response to the available experimental data. Note that also in this case the direction of the development is obtained from the assumption of an associative evolution law.

In general, all three reinforcement directions of a 3D-woven material can present non-linear viscous behaviours. In the event that experimental testing demonstrates the need for the inclusion of inelastic behaviours in the vertical weft and/or warp direction, a similar procedure as for the case of the horizontal weft directions may be followed.

4.3. Thermodynamic perspective

The choice of the components driving the development of the inelastic strain, i.e. $\boldsymbol{s}$ and $\boldsymbol{\sigma} : \boldsymbol{A}^2$, can be motivated from a thermodynamic perspective. Returning to the decomposed version of the free energy in Equation (34), the addition of the inelastic strains means that it should be expressed in terms of $\boldsymbol{e}_{el}$ and $\boldsymbol{\varepsilon}_{el}$. That is that

$$\Psi = \Psi_e(\boldsymbol{e}_{el}) + \sum_{I=1}^{3} \Psi_\varepsilon^I \left(\boldsymbol{A}^I : \boldsymbol{\varepsilon}_{el}\right), \tag{56}$$

where

$$\Psi_e = \frac{1}{2}\sum_{I=1}^{3}\phi_I \boldsymbol{A}^I : \boldsymbol{e}_{el}^2 \quad \text{and} \quad \Psi_\varepsilon^I = \frac{1}{2}\phi_I \left(\boldsymbol{A}^I : \boldsymbol{\varepsilon}_{el}\right)^2 + \frac{1}{2}\sum_{J=1}^{3}\varphi_{IJ}\left(\boldsymbol{A}^I : \boldsymbol{\varepsilon}_{el}\right)\left(\boldsymbol{A}^J : \boldsymbol{\varepsilon}_{el}\right) \tag{57}$$

Table 1

Material parameters used for the numerical example.

Stiffness	E_{11}	28 [GPa]	E_{22}	14 [GPa]	E_{33}	9 [GPa]
Shear stiffness	G_{12}	1.8 [GPa]	G_{13}^*	1.8 [GPa]	G_{23}^*	1.8 [GPa]
Poisson's ratio	ν_{12}	0.21 [-]	ν_{13}	0.30 [-]	ν_{23}	0.46 [-]

and where we again clarify that $e_{el}^2 = \boldsymbol{e}_{el} \cdot \boldsymbol{e}_{el}$.

The considered strain tensor, with the aforementioned inelastic additions, now has the following form:

$$\boldsymbol{\varepsilon} = \boldsymbol{e}_{el} + \boldsymbol{e}_i + \sum_{I=1}^{3}\left[\boldsymbol{\varepsilon}_{el} : \boldsymbol{A}^I + \varepsilon_v \boldsymbol{A}^2 : \boldsymbol{A}^I\right]\boldsymbol{A}^I. \tag{58}$$

Returning to the dissipation inequality

$$\mathscr{D} = \boldsymbol{\sigma} : \dot{\boldsymbol{\varepsilon}} - \dot{\Psi} \geq 0, \tag{59}$$

now means that expanding the first terms gives

$$\boldsymbol{\sigma} : \dot{\boldsymbol{\varepsilon}} = \boldsymbol{s} : \dot{\boldsymbol{e}}_{el} + \boldsymbol{s} : \dot{\boldsymbol{e}}_i + \sum_{I=1}^{3}\left(\boldsymbol{\sigma} : \boldsymbol{A}^I\right)\left(\dot{\boldsymbol{\varepsilon}}_{el} : \boldsymbol{A}^I\right) + \left(\boldsymbol{\sigma} : \boldsymbol{A}^2\right)\dot{\varepsilon}_v. \tag{60}$$

As in Section 3.2.4, the time derivative of the free energy is then

$$\dot{\Psi} = \frac{\partial \Psi_e}{\partial \boldsymbol{e}_{el}} : \dot{\boldsymbol{e}}_{el} + \sum_{I=1}^{3}\sum_{J=1}^{3}\frac{\partial \Psi_\varepsilon^I}{\partial\left(\boldsymbol{A}^J : \boldsymbol{\varepsilon}_{el}\right)}\left(\boldsymbol{A}^J : \dot{\boldsymbol{\varepsilon}}_{el}\right) \tag{61}$$

By inserting Equations (60) and (61) into the dissipation inequality it again follows that

$$\boldsymbol{s} = \frac{\partial \Psi_e}{\partial \boldsymbol{e}^e} \quad \text{and} \quad \boldsymbol{A}^I : \boldsymbol{\sigma} = \sum_{J=1}^{3}\frac{\partial \Psi_\varepsilon^J}{\partial\left(\boldsymbol{A}^I : \boldsymbol{\varepsilon}^e\right)}. \tag{62}$$

What remains in the reduced dissipation inequality is then

$$\mathscr{D} = \boldsymbol{s} : \dot{\boldsymbol{e}}_i + \left(\boldsymbol{A}^2 : \boldsymbol{\sigma}\right)\left(\boldsymbol{A}^2 : \dot{\boldsymbol{\varepsilon}}_i\right) \geq 0. \tag{63}$$

This reduced dissipation inequality therefore motivates why the evolution of $\boldsymbol{e}_i$ and ε_v are driven by $\boldsymbol{s}$ and $\boldsymbol{A}^2 : \boldsymbol{\sigma}$, respectively.

5. Results

Accounting for various inelastic behaviours in 3D-woven composites is a central first step to developing an accurate computational model. In order to analyse the proposed framework and the viscoelastic and crystal plasticity inspired formulations discussed in Sections 4.1 and 4.2, a 3D glass fibre reinforced epoxy composite is considered. The viscous parameters are calibrated against results from a tensile test along the horizontal weft direction as well as an Iosipescu shear test. The model is then validated against a tensile test of a specimen with a ten degree offset of the horizontal weft yarns with respect to the loading direction. This is discussed in more detail in the following section.

5.1. Summary of elastic material parameters and experimental testing

All experimental specimens were manufactured using glass fibre yarns made from HYBON 2026 XM (R-glass) 1200 Tex rovings from PPG Fiber Glass. The matrix material was selected as MTFA500 epoxy from SHD Composites. The representative volume element (RVE) size is approximately 15 mm in the warp direction, 5 mm in the horizontal weft direction and 3.9 mm in the vertical weft direction. Experimental testing in tension, compression and in-plane shear has been carried out. The in-plane tensile tests were performed according to the ASTM D3039 standard (D3039/d3039m - stan, 2013). The grip distance was approximately 60 mm for testing along the warp and approximately 70 mm for testing along the horizontal weft. Both had a width of 25 mm. The shear
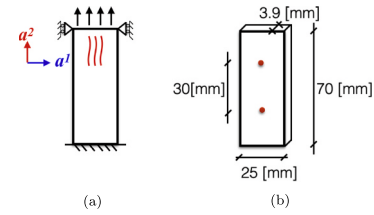

Fig. 5. Schematic showing the considered tensile specimen.

behaviour was investigated using Iosipescu tests carried out according to ASTM's V-notched shear test standard D5379 (D5379/d5379m - stan, 2017). However, given the difference between E_{11} and E_{22}, the proposed 90° angle was adjusted to 100° along with the work carried out by Melin et al. (Melin and Neumeister, 2006). In both tension and shear tests, a digital image correlation (DIC) system was used to study the displacement and strain maps on one surface of the specimens.

The obtained elastic parameters are summarised in Table 1. The out-of-plane shear moduli (marked with an asterisk) have been assumed to be equivalent to the in-plane shear modulus. Again, the warp, horizontal weft and vertical weft are denoted by 1, 2 and 3 respectively.

5.2. Calibration of the viscoelastic material parameters

The identification of the viscous parameters presented in Sections 4.1 and 4.2 is completed in two steps. As tensile testing leads to a macroscopic state of uniaxial tensile stress, this makes it possible to initially disregard the viscous parameters associated with the shear-driven slip planes. The parameters associated with the non-linear behaviour in the horizontal weft direction are therefore identified first, i.e. t_*^r, κ^r and n^r. Once they are determined, the shear related viscous parameters can be calibrated, i.e. t_*^I, κ^I and n^I. Further, the heterogeneous nature of the mesostructure will lead to strain localisation tied to the reinforcement architecture. The use of a homogeneous macroscale model does not allow for the identification of these localisation phenomena. Instead it is able to capture the overall global response of the material. For this reason, the calibration is carried out using the force-displacement response of the considered specimens.

5.2.1. Calibration of reinforcement related viscous parameters

The parameter identification routine is built around MATLAB's *fminsearch*, which uses the Nelder-Mead optimisation method (Nelder and Mead, 1965). Within *fminsearch's* objective function, the commercial finite element program Abaqus is used. In more detail, an Abaqus UMAT containing the implemented material model is opened and the viscous parameters are changed in each optimisation iteration. An input file containing a finite element model of the considered specimen is then submitted. Once the job has completed the resulting force-displacement data is extracted and compared to the experimental results. More specifically, for each time step i, the error between the experimental force, $\bar{f}$, is compared to the corresponding value extracted from the simulation, f, then normalised. The objective function that *fminsearch* seeks to minimise can then be expressed as

Table 2

Calibrated viscoelastic parameters for the non-linear response in tension along the horizontal weft.

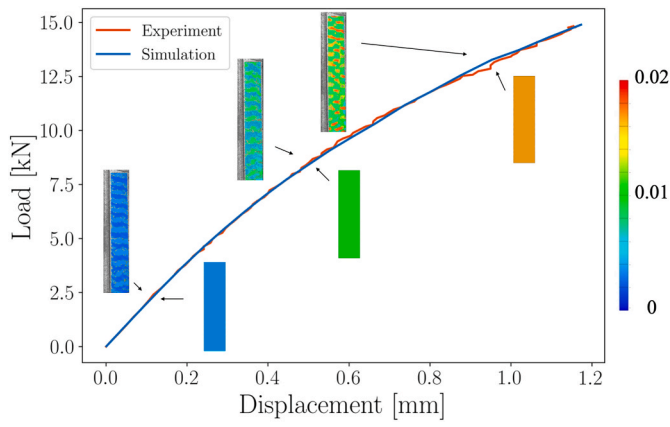| Parameter name	Value	Unit
t_*^r	$3.75 \cdot 10^7$	s
n^r	1.72	–
κ^r	1	MPa

Fig. 6. Calibrated load-displacement curve and contour plots showing axial strain distribution in the loading direction. Above the loading curve the experimental DIC results are shown while under the curve the corresponding model predictions are shown.

$$sse = \sqrt{\frac{\sum_i \left(f_i - \bar{f}_i\right)^2}{\max\left(\bar{f}_i\right)}}. \qquad (59)$$

The input file contains a three dimensional model built using fully integrated linear hexahedral elements (3DC8). Displacement driven boundary conditions on the outer edges are applied, as shown in Fig. 5a. The time history of the applied vertical displacement on the upper boundary in the model corresponds to the experimental test. More specifically, an axial strain signal is extracted from the DIC-analysis using a virtual extensometer with an initial separation of 30 mm placed approximately in the centre of the sample. Boundary conditions were applied to the model to enforce the same global strain. This corresponded to a displacement of approximately 0.7 mm/min.

The final result shows convergence of the horizontal weft related viscoelastic parameters. They are summarised in Table 2. Note that due to the nature of the proposed Norton type viscoelastic model, it is not possible to uniquely determine t_*^r and $(\kappa^r)^{n^r}$. As such it is convenient to prescribe κ^r to 1 MPa in order to maintain a dimensionless quantity within the brackets. With the obtained parameters, an analysis with a finer mesh was carried out to ensure mesh convergent results.

The obtained force-displacement curves and contour plots showing the axial strain distributions are found in Fig. 6. Both the result of the calibrated simulation and corresponding experiment are shown. Above the loading curve the experimental DIC results are shown while under the curve the corresponding model predictions are shown.
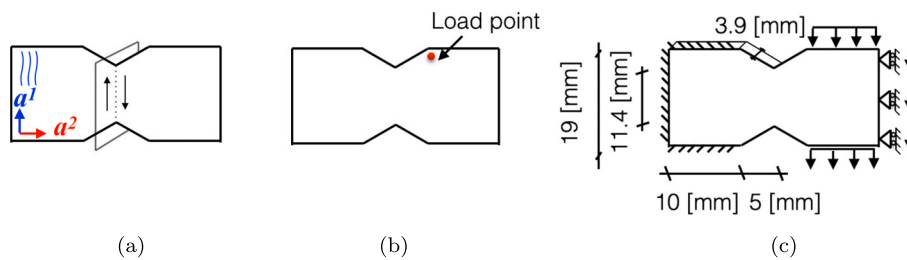
5.2.2. Calibration of shear related viscous parameters

Once t_*^r, κ^r and n^r are found, it is possible to calibrate the viscous parameters in the shear slip planes. The viscoelastic model presented in Section 4.1 generally allows for the consideration of three parameters per slip system. The focus for now, however, is given to calibrating the viscous slip parameters using an Iosipescu shear test in the plane illustrated in Fig. 7a. That is specifically, the identification of t_*^2, n^2 and again setting $\kappa^2 = 1$.

A three dimensional Abaqus model using the 3DC8 element was again used and integrated into the calibration routine based on MATLAB's *fminsearch* with the equivalent objective function presented in Equation (59). Displacement driven boundary conditions on the outer edges are applied, as shown in Fig. 7c. The time history of the vertical displacement on the right hand boundary corresponds to that measured using DIC at the indicated load point in Fig. 7b and is approximately 0.8 mm/min.

Fig. 8 again shows the resulting force-displacement curves and shear strain distributions for the calibrated model and the corresponding Iosipescu shear experiment. The images above the curve again
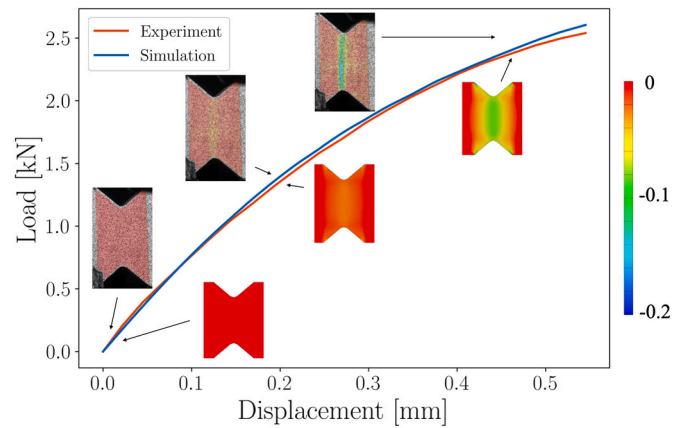

Fig. 8. Calibrated load-displacement curve and contour plots showing in plane shear strain. Above the loading curve the experimental DIC results are shown while under the curve the corresponding model predictions are shown.

Table 3
Calibrated viscoelastic parameters for the non-linear response in shear.

Parameter name	value	Unit
t_*^2	$6.46 \cdot 10^5$	s
n^2	1.538	–
κ^2	1	MPa

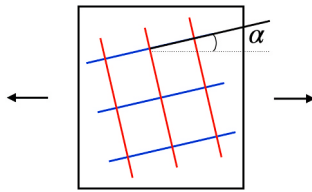**Fig. 7.** Schematic showing the considered shear specimen.

Fig. 9. Illustration of the orientation of the reinforcement directions with respect to the loading directions.

correspond to the experimental DIC results of the experiments while the images below the curve show the model prediction. Note that the experimental results are shown and calibrated until the first load drop. The obtained parameters are presented in Table 3.

As previously discussed the nature of this approach does not allow for the identification of strain localisation behaviours. While the overall global response can be accurately captured by the proposed model both in the case of tensile loading in the horizontal weft direction (Fig. 6) and in shear (Fig. 8), obtaining an equally exact comparison of the axial and shear strain distributions is challenging.

5.3. Overview of the model response

To demonstrate the main characteristics of the proposed model, the case of uniaxial stress at the material point level is considered. Various orientations α of the fibre reinforcements are evaluated, as shown in Fig. 9. The viscous parameters are taken from Sections 5.2.1 and 5.2.2 and an equivalent loading rate to that used during experimental testing is considered. Fig. 10a shows the material response under tensile loading for varying in-plane orientations of the fibre reinforcement. Loading along the direction of the warp yarns, i.e. α = 0°, produces a linear elastic response, that gradually softens until reaching an orientation of α = 45°. Continuing past α = 45°, shown in Fig. 10b, gradually stiffens the resulting behaviour until reaching the case of tensile loading along the direction of the horizontal weft reinforcement, at α = 90°.

5.4. Prediction of off-axis tensile test

Model validation was carried out by considering a tensile specimen with the horizontal weft reinforcement oriented at a ten degree offset to the loading direction, i.e. α = 100°. Testing was carried out according to the ASTM D3039 standard with a grip distance of 60 mm and a specimen width of 15 mm. A three dimensional FE model using fully integrated linear hexahedral elements was again constructed in Abaqus, with displacement driven boundary conditions as shown in Fig. 11a. The magnitude of the applied boundary conditions was determined based on the DIC data of the corresponding experiment. Specifically, a virtual extensometer, with an initial separation of 30 mm was used to extract

the axial strain measurements. The extensometer was placed over the approximate centre of the specimen, shown in Fig. 11b. Based on the length of the specimen, comparable boundary conditions to achieve the same global strain were applied. This corresponded to a displacement of approximately 1.3 mm/min.

The experimental cyclic load-displacement behaviour for the considered off-axis specimen is shown in Fig. 12. Currently, focus is given to evaluating the predicted material response under monotonic loading, again shown in Fig. 12. The initial global response of the material can be predicted with fair agreement, until the point that damage is visible in the DIC images. The model however showed a limited ability to predict the unloading behaviour of the test specimen, and is a place for future improvements and developments. Initial inconsistencies in the stiffness of the experimental and simulation results may be due to variations in the loading rate of the on and off-axis specimens. The nature of macroscale models again means that localised strains are not possible to capture.
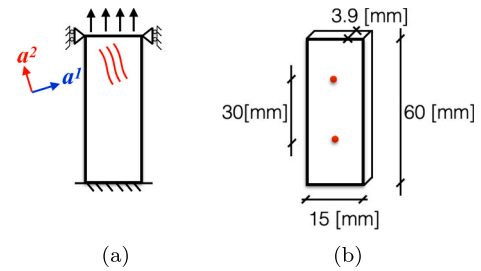

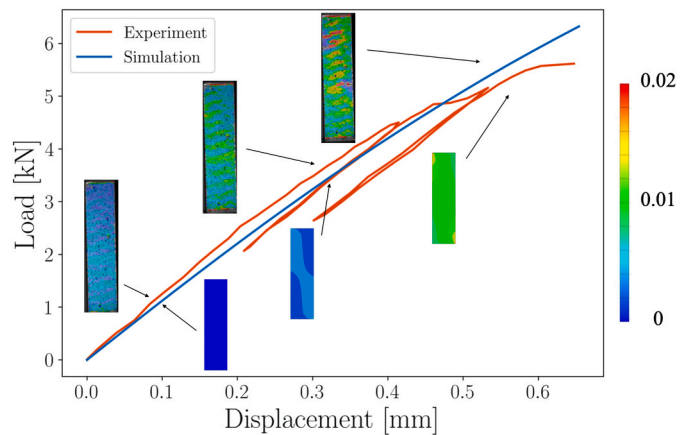**Fig. 11.** Schematic showing the considered off-axis tensile specimen.

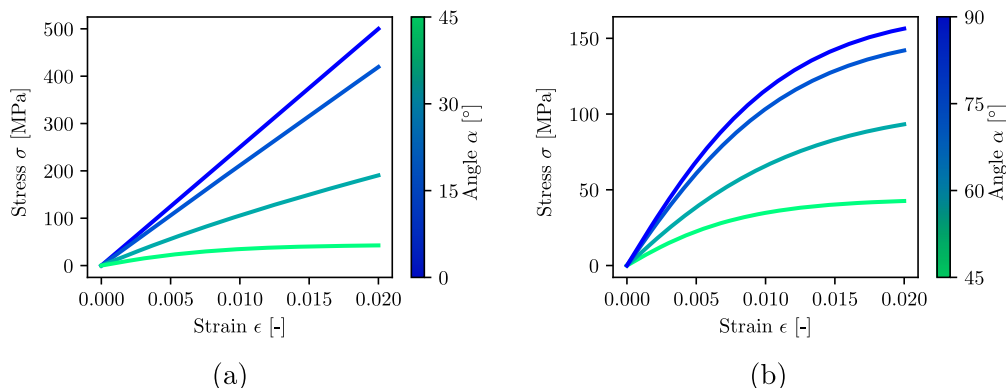**Fig. 12.** Load-displacement curve of experimental and predicted results.

Fig. 10. Stress-strain curves under uniaxial stress for varying reinforcement orientations.

6. Conclusions

Composite materials with 3D-woven reinforcements have shown a number of promising characteristics over their laminated counterparts. This includes improved out-of-plane properties, damage tolerance and increased specific energy absorption. In order to allow for their widespread adoption in industry however, efficient computational models are required. The current contribution proposes a framework for modelling the mechanical response of 3D-woven composites on the macroscale. The framework is based on a decomposition of the stress and strain tensor, assuming three nominal reinforcement directions, analogous to the propositions for unidirectional composites (with one reinforcement direction) by Spencer (1984) and Nedjar (2011). By adopting these stress and strain tensor decompositions, the modelling framework conveniently allows for the separation of the model response into two parts. Specifically, one which is related to the behaviour of the reinforcement directions while the other is related to shear.

The proposed framework was applied to the case of a 3D-woven glass fibre reinforced epoxy material. This material showed a prominent non-linear response when loaded both in shear and in tension along the horizontal weft. In order to mimic the observed non-linear monotonic loading curve, a Norton viscoelasticity model was adopted as an initial starting point. In particular, under shear loading, the Norton model was combined with a crystal plasticity inspired approach. The viscous parameters were successfully calibrated against experimental results. Validation of the model was carried out by considering off-axis tensile testing and showed fair agreement.

The presented framework is general, thermodynamically consistent and it allows for the addition of various experimentally observed inelastic phenomena in a modular fashion, based on loading direction. This provides a clear calibration scheme which links parameters to distinct experimental tests, simplifying material parameter identification. Furthermore, we note that it has a straightforward extension to the case of finite strains, to incorporate effects such as reinforcement rotation and (thereby) stretching under large shear deformation.

Declaration of competing interest

The authors declare that they have no known competing financial interests or personal relationships that could have appeared to influence the work reported in this paper.

Acknowledgements

References

Ansar, M., Xinwei, W., Chouwei, Z., 2011. Modeling strategies of 3D woven composites: a review. Compos. Struct. 93, 1947–1963.

Brown, L.P., Sherburn, M., 2017. Texgen v3.9.0. Zenodo.

Camanho, P.P., Arteiro, A., Melro, A.R., Catalanotti, G., Vogler, M., 2015. Three-dimensional invariant-based failure criteria for fibre-reinforced composites. Int. J. Solid Struct. 55, 92–107.

Cox, B.N., Dadkhah, M.S., Morris, W.L., 1996. On the tensile failure of 3D woven composites. Compos. Appl. Sci. Manuf. 27, 447–458.

ASTM, 2013. D3039/d3039m - Standard Test Method for Tensile Properties of Polymer Matrix Composite Materials.

ASTM, 2017. D5379/d5379m - Standard Test Method for Shear Properties of Composite Materials by the V-Notched Beam Method.

Dahale, M., Neale, G., Lupicini, R., Cascone, L., McGarrigle, C., Kelly, J., Archer, E., Harkin-Jones, E., McIlhagger, A., 2019. Effect of weave parameters on the mechanical properties of 3D woven glass composites. Compos. Struct. 223, 110947.

Ekermann, T., Hallström, S., 2015. Mechanical characterisation of composites with 3D-woven reinforcement. In: 20th International Conference on Composite Materials, pp. 19–24.

El Said, B., Daghia, F., Ivanov, D., Hallett, S.R., 2018. An iterative multiscale modelling approach for nonlinear analysis of 3D composites. Int. J. Solid Struct. 132–133, 42–58.

Green, S.D., Matveev, M.Y., Long, A.C., Ivanov, D., Hallett, S.R., 2014. Mechanical modelling of 3D woven composites considering realistic unit cell geometry. Compos. Struct. 118, 284–293.

Hill, R., 1966. Generalized constitutive relations for incremental deformation of metal crystals by multislip. J. Mech. Phys. Solid. 14, 95–102.

Hirsekorn, M., Marcin, L., Godon, T., 2018. Multi-scale modeling of the viscoelastic behavior of 3D woven composites. Compos. Appl. Sci. Manuf. 112, 539–548.

Khokar, N., 2001. 3D-Weaving: theory and practice. J. Textil. Inst. 92, 193–207.

Khokar, N., Winberg, F., Hallström, S., 2015. Novel 3D preform architecture for performance and reliability of structural beams. In: ICCM International Conferences on Composite Materials, pp. 19–24.

Larijani, N., Johansson, G., Ekh, M., 2013. Hybrid microemacromechanical modeling of anisotropy evolution in pearlitic steel. Eur. J. Mech. Solid. 38, 38–47.

Lomov, S.V., Gusakov, A.V., Huysmans, G., Prodromou, A., Verpoest, I., 2000. Finite element modelling of progressive damage in non-cimp 3D orthogonal weave and plain weave E-glass composites. Compos. Sci. Technol. 60, 2083–2095.

Lomov, S.V., Ivanov, D.S., Verpoest, I., Zako, M., Kurashiki, T., Nakai, H., Hirosawa, S., 2007. Meso-FE modelling of textile composites: road map, data flow and algorithms. Compos. Sci. Technol. 67, 1870–1891.

Marcin, L., Carrère, N., Maire, J.F., 2008. A macroscopic visco-elastic-damage model for three-dimensional woven fabric composites. In: Proceeding of ECCM13 - 13th European Conference on Composite Materials.

Melin, L.N., Neumeister, J.M., 2006. Measuring constitutive shear behavior of orthotropic composites and evaluation of the modified Iosipescu test. Compos. Struct. 76, 106–115.

Nagaraja, S.G., Pletz, M., Schuecker, C., 2019. Constitutive modeling of anisotropic plasticity with application to fiber-reinforced composites. Int. J. Solid Struct. 180–181, 84–96.

Nedjar, B., 2011. A time dependent model for unidirectional fibre-reinforced composites with viscoelastic matrices. Int. J. Solid Struct. 48, 2333–2339.

Nelder, J., Mead, R., 1965. A simplex method for function minimization. Comput. J. 7, 308–313.

Norton, F., 1929. The Creep of Steels at High Temperatures. McGraw-Hill Book Company.

Saseendran, S., Wysocki, M., Varna, J., 2016. Evolution of viscoelastic behavior of a curing LY5052 epoxy resin in the glassy state. Adv. Manuf. Polym. Compos. Sci. 2, 74–82.

Spencer, A., 1984. Continuum Theory of the Mechanics of Fibre-Reinforced Composites. Springer-Verlag.

Stig, F., Hallström, S., 2009. Assessment of the mechanical properties of a new 3D woven fibre composite material. Compos. Sci. Technol. 69, 1686–1692.

Stig, F., Hallström, S., 2012. Spatial modelling of 3D-woven textiles. Compos. Struct. 94, 1495–1502.

Stig, F., Hallström, S., 2019. Effects of crimp and textile architecture on the stiffness and strength of composites with 3D reinforcement. Adv. Mater. Sci. Eng. 2019.

Tong, L., Tan, P., Steven, G.P., 2002. Effect of yarn waviness on strength of 3D orthogonal woven CFRP composite materials. J. Reinforc. Plast. Compos. 21, 153–173.

Vogler, M., Rolfes, R., Camanho, P.P., 2013. Modeling the inelastic deformation and fracture of polymer composites-Part I: plasticity model. Mech. Mater. 59, 50–64.

Warren, K.C., Lopez-Anido, R.A., Goering, J., 2015. Experimental investigation of three-dimensional woven composites. Compos. Appl. Sci. Manuf. 73, 242–259.

Whitney, T.J., Chou, T., 1988. Modeling textile structural composites rcomposite. J. Compos. Mater. 890–911.

Woo, E.M., Seferis, J.C., Schaffnit, R.S., 1991. Viscoelastic characterization of high performance epoxy matrix composites. Polym. Compos. 12, 273–280.

Xia, Q.S., Boyce, M.C., Parks, D.M., 2002. A constitutive model for the anisotropic elastic – plastic deformation of paper and paperboard. Int. J. Solid Struct. 39, 4053–4071.

Yushanov, S., Bogdanovich, A., 1999. Manufacturing and property analysis of a novel class of 3-D woven composites. J. Thermoplast. Compos. Mater. 12, 70–82.